Acta Cryst. (1988). A44, 383-391

Streaks of Instrumental Origin Near a Bragg Point

BY S. A. WERNER AND M. ARIF

Department of Physics and Astronomy, University of Missouri-Columbia, Columbia, MO 65211, USA

(*Received* 8 *September* 1987; *accepted* 25 *January* 1988)

Abstract

It is predicted that, at some sufficiently high level of sensitivity, two streaks intersecting at the Bragg point and symmetrically situated about the reciprocal-lattice vector **G** should always be observable in a diffraction experiment.

Introduction

We show here that the close examination of a Bragg point G in any diffraction experiment will reveal the presence of two streaks, intersecting at G and symmetrically situated about the radial line leading from the origin of reciprocal space to the point G, as shown in Fig. 1. The angle χ between the two streaks will depend upon the instrumental parameters as discussed below, but can be expected to approach $2\theta_B$ in most cases. We believe that the occurrence of these streaks is a very general instrumental phenomenon, and will be observed at some level of sensitivity in all experiments. Our thinking here is guided by experience with high-resolution high-sensitivity triple-axis neutron diffraction experiments, which can routinely be carried out in the sensitivity range of 10^{-4} to 10^{-6} of the Bragg point intensity. The reasoning and analysis given here apply equally well to high-sensitivity X-ray diffraction experiments, such as those designed to examine Huang scattering or thermal diffuse scattering (TDS).

We label the two streaks type I and type II. The occurrence of the type I streak is well known, although its physical origin is rarely examined in any detail. It occurs when the Bragg point G falls on the sphere of reflection, giving a strong reflected beam at a scattering angle $2\theta = 2\theta_B$, but the detector is situated at an angle γ away from the nominal scattering angle $2\theta_B$ that is required to fully accept this Bragg beam (Fig. 2). Normally, if γ is several times the resolution

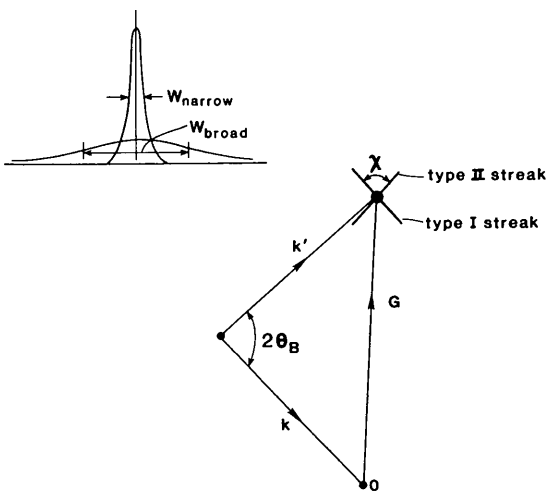

$$\tan\frac{\chi}{2} = \left(\frac{1-\rho_0^2}{1+\rho_0^2}\right)\tan\theta_B$$

$$\rho_0 = W_{narrow}/W_{broad}$$

Fig. 1. Orientation of instrumentally generated streaks in reciprocal space.

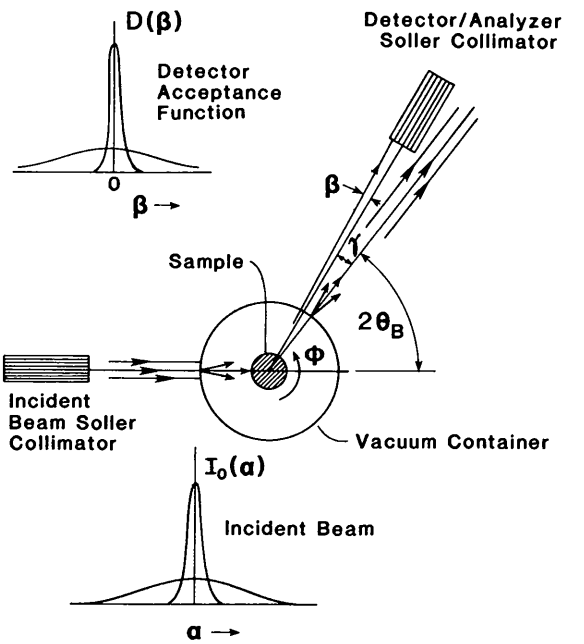

Fig. 2. Schematic diagram of typical diffraction experiment, showing the possibility of small-angle scattering of the incident and diffracted beams by the vacuum container surrounding the sample. The small-angle scattering has the effect of creating an incident beam $I_0(\alpha)$ having a broad component in addition to the original narrow component. Small-angle scattering in the diffracted beam leads to a detector acceptance function $D(\beta)$ having a broad component in addition to a narrow component.

0108-7673/88/030383-09$03.00

width of the detector Soller collimator, we assume that few, if any, Bragg-reflected neutrons will be counted. However, we know that at some level of sensitivity some neutrons will penetrate through the Soller blades and be reflected by the tail of the analyzer crystal's mosaic distribution. We claim, therefore, for this reason at least, that the detector/analyzer acceptance function $D(\beta)$ will involve two parts: a very narrow part due to neutrons passing directly through the Soller slits, and a much broader part due to neutrons penetrating the Soller blades. This is shown in Fig. 2. There are other physical origins of the broad part of $D(\beta)$. For example, the neutron when penetrating the sample capsule, cryostat heat shields or vacuum container will suffer small-angle scattering, thus broadening the narrow distribution of Bragg-reflected neutrons. At some level of sensitivity air scattering will also play a role. The neutrons being counted due to the broad part of $D(\beta)$ appear as a streak of type I in reciprocal space, as shown in Fig. 1.

We now show that there is another streak (type II) situated symmetrically with respect to the reciprocal-lattice line OG. The angular distribution of incident neutrons $I_0(\alpha)$ must also have two parts (a narrow component and a broad component) for the same physical reasons mentioned above. That is, some small fraction of the neutrons leaving the monochromator will penetrate through the Soller blades, and/or be small-angle scattered on their trajectory to the sample. For simplicity, let us first suppose that all neutrons are of a given fixed wave vector k_0. Thus, the Bragg angle is a very definite angle $\theta_B^0 = \sin^{-1}(G/2k_0)$. Let us also suppose that the sample is a perfect single crystal. Thus, a Bragg scattering process takes an incident neutron at angle α [with probability $I_0(\alpha)$] and reflects it to an angle $2\theta_B^0 + \alpha$ at which point it is counted with probability $D(\beta)$, where $\beta = \alpha - \gamma$. It is easy to see from the Bragg-scattering triangle that, for a neutron in the incident beam at angle α to be Bragg scattered by a perfect crystal, the crystal must be rotated by an angle $\varphi = \alpha$, and thus $\beta = \varphi - \gamma$. Consequently, the scattered intensity $I_s(\varphi, \gamma)$ as a function of crystal setting φ and detector setting γ is simply

$$I_s(\varphi, \gamma) = W_0 I_0(\varphi) D(\varphi - \gamma), \tag{1}$$

where W_0 is the probability for Bragg scattering. The Bragg scattering process thus acts as a caliper between the incident distribution $I_0(\alpha)$ and the detector acceptance function $D(\beta)$ as shown in Fig. 3. We see from this figure that (for fixed γ) as the left marker of the caliper moves through the sharp peak of $I_0(\alpha)$ (as φ is varied) the right marker moves along the broad part of $D(\beta)$, giving rise to a sharp low-intensity peak at $\varphi = 0$. This is the type-I streak. Likewise, as the right marker moves through the sharp component of $D(\beta)$ as φ is increased, the left marker moves along the broad part of $I_0(\alpha)$, giving rise to another sharp low-intensity peak at $\varphi = \gamma$. This is the type II streak. The apparent orientation of these streaks in reciprocal space is obtained by noting that

$$\Delta Q_y = (\gamma G/2) \cot \theta_B \tag{2}$$

and

$$\Delta Q_x = (G/2)(\gamma - 2\varphi), \tag{3}$$

as shown in Fig. 4. Here $\hat{\mathbf{y}}$ is along $\mathbf{G}$ and $\hat{\mathbf{x}}$ is perpendicular to $\mathbf{G}$, and the nominal spectrometer scattering vector $\mathbf{Q} = \Delta\mathbf{Q} + \mathbf{G}$. Thus for a type-I streak

$$\varphi = 0, \qquad \Delta Q_y / \Delta Q_x = \cot \theta_B, \tag{4}$$

and for a type-II streak

$$\varphi = \gamma, \qquad \Delta Q_y / \Delta Q_x = -\cot \theta_B. \tag{5}$$

Thus, the angle χ between the streaks shown in Fig. 1 is $2\theta_B$.

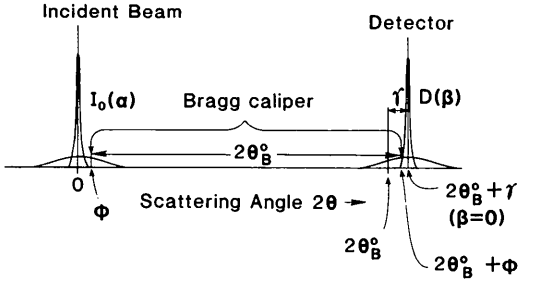

Fig. 3. Diagram showing how the Bragg scattering process acts as a caliper of fixed 'length' $2\theta_\beta^\circ$ on the scattering-angle scale, carrying neutrons from a point $\alpha = \varphi$ on the incident-beam distribution to a point $2\theta_\beta + \varphi$ on the detector acceptance function distribution.

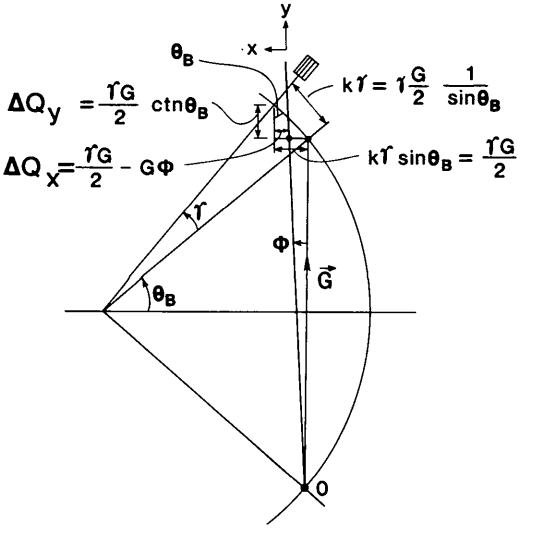

Fig. 4. Drawing to show how the spectrometer setting $(\Delta Q_x, \Delta Q_y)$ relative to the Bragg point G depends on the crystal angle φ and the detector setting γ.

Effect of sample mosaic spread

We now attempt to model these processes in a more general and precise manner, taking into account first the finite mosaic spread of the sample crystal. The beam emerging from the monochromator assembly and incident upon the sample is distributed in a small region of **k** space surrounding the nominal incident wave vector $\mathbf{k}_i$ shown in Fig. 5. We represent this by the sum of two ellipsoidal distributions, one narrow and one broad. Similarly the acceptance function of the detector/analyzer system is the sum of two distributions, one narrow and one broad, centered on the nominal wave vector $\mathbf{k}_f$. Neutrons in the incident distribution $I_0(\Delta\mathbf{k}_i)$ are carried to the detector distribution $D(\Delta\mathbf{k}_f)$ by Bragg scattering in the sample crystal. In order to calculate the counting rate $I_s(\varphi, \gamma)$ as a function of crystal angle φ and detector angle γ, we regard the center of neutron **k** space as the origin of coordinates, as shown in Fig. 5. That is, the origin of the crystal's reciprocal lattice is allowed to move as a function of φ in this diagram. The advantage of this is shown in Fig. 6. A perfect crystal set at $\varphi = 0$ scatters incident neutrons from the line A-A to the line B-B. Rotating the crystal through an angle φ then allows the Bragg scattering process to transfer neutrons from a line A'-A' (nearly parallel to A-A) to line B'-B' (nearly parallel to B-B). We now use this fact and Fig. 5 to calculate $I_s(\varphi, \gamma)$.

We assume that $I_0(\Delta\mathbf{k}_i)$ is the sum of two Gaussian functions and likewise that $D(\Delta\mathbf{k}_f)$ is the sum of two other Gaussian functions. For simplicity, we first assume that the incident beam is nearly monochromatic. (In the next section we will relax this requirement.) Then, for a given setting of the crystal φ, the counting rate will depend upon the product of these functions, each integrated along the k_x axis. We thus need only

$$I_0(\Delta k_{iy}) = \int I_0(\Delta k_{ix}, \Delta k_{iy})\, \mathrm{d}(\Delta k_{ix}) \tag{6}$$

and

$$D(\Delta k_{fy}) = \int D(\Delta k_{fx}, \Delta k_{fy})\, \mathrm{d}(\Delta k_{fx}). \tag{7}$$

It is only the projection of the wave vectors onto the y axis that enters this calculation. A diagram which is the analog of Fig. 3 is shown in Fig. 7. The 2θ axis is replaced by K_y, and we have allowed the crystal to have a Gaussian distribution with a mosaic spread parameter η. The following definitions are useful:

$$M \equiv \tfrac{1}{2}G(\cot\theta_B)\eta, \tag{8}$$

$$\Phi \equiv \tfrac{1}{2}G(\cot\theta_B)\varphi \tag{9}$$

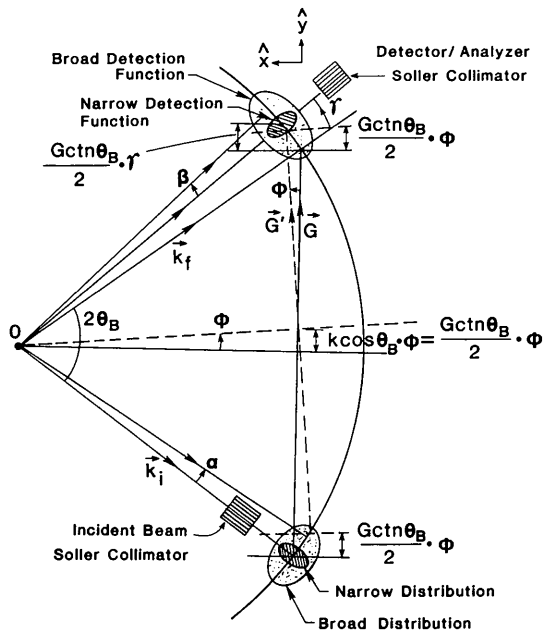

Fig. 5. Diagram showing the narrow and broad distributions of incident neutrons, and how they are connected by the Bragg scattering process to the narrow and broad parts of the detector/analyzer acceptance function.

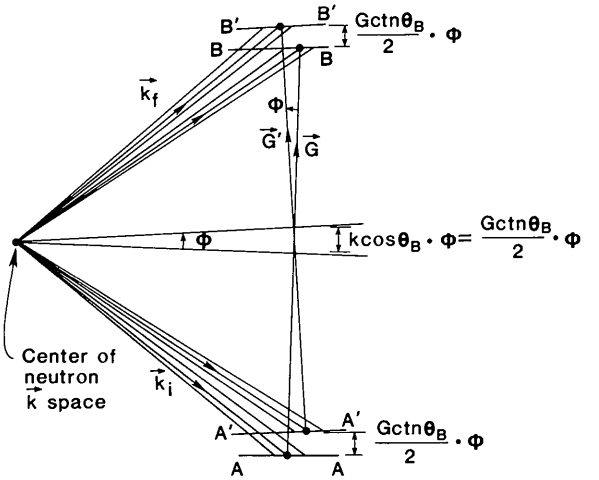

Fig. 6. A perfect crystal Bragg scatters neutrons distributed on the line A-A to the line B-B in **k** space. When the crystal is rotated through a small angle φ, the Bragg scattering process then carries neutrons from the line A'-A' to the line B'-B'.

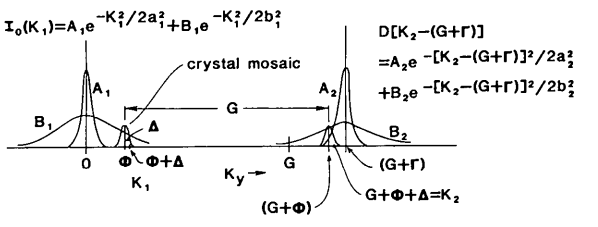

Fig. 7. This diagram is analogous to Fig. 3, except that the 2θ axis is rescaled to be a wave vector K_y, where $\hat{\mathbf{y}}$ is along **G**; and the sample crystal has a mosaic width. This diagram is used in deriving the expressions for the intensity $I_s(\Phi, \Gamma)$ given by equations (11) and (19).

and

$$\Gamma \equiv \tfrac{1}{2}G(\cot\theta_B)\gamma. \tag{10}$$

The width parameter a_1 of the narrow part of $I_0(\alpha)$ is directly related to the monochromator mosaic spread and its collimation. The width parameter a_2 of the narrow part of $D(\beta)$ is calculable from the analyzer mosaic spread and its associated collimation. The width parameters b_1 and b_2 depend upon the physical origin of the broad distributions. The counting rate is easily seen to be

$$I_s(\Phi,\Gamma) = \int I_0(K_1)\, W(K_1 \to K_2) \times D(K_2 - G - \Gamma)\, dK_1\, dK_2, \tag{11}$$

where

$$W(K_1 \to K_2) = W_0 \exp(-\Delta/2M^2)\delta(K_2 - K_1 - G), \tag{12}$$

and

$$I_0(K_1) = A_1 \exp(-K_1^2/2a_1^2) + B_1 \exp(-K_1^2/2b_1^2), \tag{13}$$

and

$$D(K_2 - G - \Gamma) = A_2 \exp[-(K_2 - G - \Gamma)^2/2a_2^2] + B_2 \exp[-(K_2 - G - \Gamma)^2/2b_2^2]. \tag{14}$$

We find after integrating over the delta function in (12) that

$$K_1 = \Phi + \Delta \tag{15}$$

and

$$K_2 = G + K_1 = G + \Phi + \Delta. \tag{16}$$

The wave vector Δ is related to the mosaic angle δ by

$$\Delta = \tfrac{1}{2}G(\cot\theta_B)\delta, \tag{17}$$

where the Gaussian distribution of the orientation of mosaic grains is

$$W(\delta) = (2^{1/2}\pi\eta)^{-1} \exp(-\delta^2/2\eta^2). \tag{18}$$

Thus, we have to evaluate the single integral

$$I_s(\Phi,\Gamma) = \int I_0(\Phi + \Delta)\, W_0 \exp(-\Delta^2/2M^2) \times D(\Phi + \Delta - \Gamma)\, d\Delta. \tag{19}$$

This result is identical to (1), except that now we must integrate over the mosaic distribution of the sample. The integral (19) involves four terms, each a Gaussian integral which can be explicitly carried out. The nominal spectrometer setting in reciprocal space is given by $(\Delta Q_x, \Delta Q_y)$, where, according to (2) and (3),

$$\Phi = \tfrac{1}{2}(\Delta Q_y - \cot\theta_B \Delta Q_x) \tag{20}$$

and

$$\Gamma = \Delta Q_y. \tag{21}$$

Table 1. *Summary of Gaussian parameters*

Main Bragg peak, very strong ($i=0$)	Broad Bragg peak, very weak ($i=2$)
$N_0 = \left(\frac{2\pi}{2+\rho_1^2}\right)^{1/2} W_0 A^2$	$N_3 = b\left(\frac{2\pi}{2+\rho_2^2}\right)^{1/2} W_0 B^2$
$\sigma_0 = 2a\tan\theta_B\left(\frac{2+\rho_1^2}{2\rho_1^2}\right)^{1/2}$	$\sigma_3 = 2b\tan\theta_B\left(\frac{2+\rho_2^2}{2\rho_2^2}\right)^{1/2}$
$\mu_0 = (2^{1/2})a$	$\mu_3 = (2^{1/2})b$
$S_0 = 0$	$S_3 = 0$
Type-I streak ($i=1$)	**Type-II streak ($i=2$)**
$N_1 = a\left(\frac{2\pi}{1+\rho_0^2+\rho_1^2}\right)^{1/2} W_0 AB$	$N_2 = a\left(\frac{2\pi}{1+\rho_0^2+\rho_1^2}\right)^{1/2} W_0 AB$
$\sigma_1 = 2a\tan\theta_B\left(\frac{1+\rho_0^2+\rho_1^2}{\rho_1^2+\rho_0^2\rho_1^2}\right)^{1/2}$	$\sigma_2 = 2a\tan\theta_B\left(\frac{1+\rho_0^2+\rho_1^2}{\rho_1^2+\rho_0^2\rho_1^2}\right)^{1/2}$
$\mu_1 = b$	$\mu_2 = b$
$S_1 = \left(\frac{1-\rho_0^2}{1+\rho_0^2}\right)\tan\theta_B$	$S_2 = -\left(\frac{1-\rho_0^2}{1+\rho_0^2}\right)\tan\theta_B$

Thus, we can write an explicit expression for the counting rate at a spectrometer setting $(\Delta Q_x, \Delta Q_y)$:

$$I_s(\Delta Q_x, \Delta Q_y) = \sum_{i=0}^{3} N_i \exp\left[-\frac{(\Delta Q_x - S_i \Delta Q_y)^2}{2\sigma_i^2} - \frac{(\Delta Q_y)^2}{2\mu_i^2}\right]. \tag{22}$$

For simplicity in quoting the results for the parameters N_i, S_i, σ_i and μ_i, we assume that the spectrometer is symmetrically configured, such that $a \equiv a_1 = a_2$, $b \equiv b_1 = b_2$, $A \equiv A_1 = A_2$ and $B \equiv B_1 = B_2$. We define the ratio of the width of the narrow distribution to the width of the broad distribution as

$$\rho_0 \equiv a/b, \tag{23}$$

and the ratios of the widths of the narrow distribution and the broad distribution to the crystal mosaic width (M) as

$$\rho_1 = a/M \tag{24}$$

and

$$\rho_2 = b/M. \tag{25}$$

Table 1 gives a summary of the results for the Gaussian parameters entering (22). The slope $(\Delta Q_x/\Delta Q_y)$ of the type-I streak is S_1 and of the type-II streak is S_2. Thus, the angle χ between the type-I and type-II streaks is given by

$$\tan(\chi/2) = \left(\frac{1-\rho_0^2}{1+\rho_0^2}\right)\tan\theta_b. \tag{26}$$

The angle χ will always be less than $2\theta_B$.

When the crystal mosaic spread is small, the width of a transverse scan through the main Bragg peak is $\sigma_0 = 2^{1/2}a\tan\theta_B$, while the width of a transverse scan through one of the streaks is $\sigma_1 = \sigma_2 = 2a\tan\theta_B$; that is, a factor of $2^{1/2}$ broader.

Effect of wavelength spread

It is well known that the angle-wavelength correlation in a beam produced or analyzed by Bragg scattering in crystals creates complicated, and sometimes surprising, resolution effects in triple-axis neutron and X-ray scattering experiments. In this section we take these correlations into account. At the same time, we will also model the effects of the small-angle scattering taking place in the incident beam before reaching the sample crystal, and likewise the small-angle scattering affecting the diffracted beam before entering the analyzer system shown in Fig. 2. The analysis is rather cumbersome algebraically, but straightforward. The result of this calculation is the general elastic resolution function of a triple-axis spectrometer. We will find that the results of the previous section are qualitatively correct, though numerically only approximate. The resolution function for an X-ray triple-axis spectrometer has recently been discussed by Cowley (1987). The analysis here is considerably more complicated because it takes into account the effects of small-angle scattering in the incident and diffracted beams.

The beam incident upon the sample is distributed over a small volume in $\mathbf{k}$ space (centered at $\mathbf{k}_i^0$) described by the function $I_0(\Delta\mathbf{k}_i)$, where

$$\Delta\mathbf{k}_i = \mathbf{k}_i - \mathbf{k}_i^0, \tag{27}$$

and the analyzer/detector system accepts scattered neutrons within a small volume in $\mathbf{k}$ space (centered at $\mathbf{k}_f^0$) described by the function $D(\Delta\mathbf{k}_f)$, where

$$\Delta\mathbf{k}_f = \mathbf{k}_f - \mathbf{k}_f^0. \tag{28}$$

Bragg scattering by the sample carries neutrons from a point $\Delta\mathbf{k}_i$ within the first volume to a point $\Delta\mathbf{k}_f$ with probability density $W(\Delta\mathbf{k}_i \to \Delta\mathbf{k}_f)$. Thus, the counting rate at a given setting $(\Delta Q_x, \Delta Q_y)$ of the spectrometer is given by

$$I_s(\Delta Q_x, \Delta Q_y) = \int I_0(\Delta\mathbf{k}_i)\, W(\Delta\mathbf{k}_i \to \Delta\mathbf{k}_f) D(\Delta\mathbf{k}_f) \times \mathrm{d}(\Delta k_{ix})\, \mathrm{d}(\Delta k_{iy})\, \mathrm{d}(\Delta k_{fx})\, \mathrm{d}(\Delta k_{fy}). \tag{29}$$

This four-dimensional integral is the generalization of the two-dimensional integral, (11), of the previous section. For Bragg scattering in a mosaic grain oriented at an angle specified by Δ, in a crystal oriented at an angle specified by Φ, with the detector/analyzer system set at an angle specified by Γ, we find with the help of Figs. 4 and 5 that

$$\Delta k_{fy} = \Delta k_{iy} - \Gamma, \tag{30}$$

$$\Delta k_{fx} = \Delta k_{ix} + \tan\theta_B[2\Phi + 2\Delta - \Gamma], \tag{31}$$

and

$$\Delta = \Delta k_{iy} - \Phi. \tag{32}$$

Thus the function $W(\Delta\mathbf{k}_i \to \Delta\mathbf{k}_f)$ contains two delta functions, and it is explicitly given by

$$W(\Delta\mathbf{k}_i \to \Delta\mathbf{k}_f) = W_0 \exp[-(\Delta k_{iy} - \tfrac{1}{2}\Delta Q_y + \tfrac{1}{2}\cot\theta_s \Delta Q_x)^2/2M^2] \times \delta(\Delta k_{fy} - \Delta k_{iy} + \Delta Q_y)\delta(\Delta k_{fx} - \Delta k_{ix} - 2\tan\theta_s \Delta k_{iy} + \tan\theta_s \Delta Q_y), \tag{33}$$

where we have used (20) and (21) to replace Φ and Γ by ΔQ_x and ΔQ_y. As in the previous section, we assume that $I_0(\Delta\mathbf{k}_i)$ consists of two parts. Here we explicitly assume that the narrow part is due to the intense beam arriving at the sample without suffering any small-angle scattering, while the broad weak part is due to the fraction of the incident beam which penetrates the Soller slits or experiences small-angle scattering in the cryostat vacuum can, heat shield or sample capsule before striking the sample.

We first describe $I_0(\Delta\mathbf{k}_i)$ in the primed coordinate frame shown in Fig. 8, where $\hat{\mathbf{x}}'$ is antiparallel to $\mathbf{k}_i$ and $\hat{\mathbf{y}}'$ is perpendicular to $\mathbf{k}_i$. The narrow (n) intense part of $I_0(\Delta\mathbf{k}_i)$ is of the form

$$I_0^n(\Delta\mathbf{k}_i) = t_0 I_0 \exp(-\tfrac{1}{2}H_{in}) \tag{34}$$

where H_{in} is of the biquadratic form

$$H_{in} = a'_{in}\Delta k_{ix'}^2 + b'_{in}\Delta k_{ix'}\Delta k_{iy'} + c'_{in}\Delta k_{iy'}^2. \tag{35}$$

The subscript i signifies the incident beam, and the subscript n denotes the narrow part of the incident-beam distribution in $\mathbf{k}$ space. The coefficients a'_{in}, b'_{in} and c'_{in} are related to the Gaussian parameters α_0, α_1 and η_m characterizing the source-to-monochromator and monochromator-to-sample collimations and the monochromator mosaic spread respectively. Using the results of the paper by Werner & Pynn (1971), we can write

$$a'_{in} = \frac{\sin^2 2\theta_m}{k_0^2\alpha_0^2} + \frac{\tan^2\theta_m}{k_0^2\eta_m^2}, \tag{36}$$

$$b'_{in} = \frac{\sin 4\theta_m}{k_0^2\alpha_0^2} + \frac{2\tan\theta_m}{k_0^2\eta_m^2} \tag{37}$$

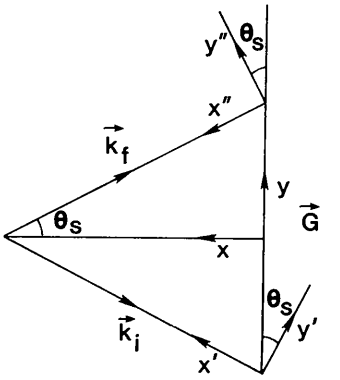

Fig. 8. Coordinate frames used in writing the components of $\Delta\mathbf{k}_i$ and $\Delta\mathbf{k}_f$.

and

$$c'_{in}=\frac{\cos^2 2\theta_m}{k_0^2\alpha_0^2}+\frac{1}{k_0^2\alpha_1^2}+\frac{1}{k_0^2\eta_m^2}. \tag{38}$$

The coefficient t_0 specifies the fraction of the incident beam transmitted directly to the sample crystal without being affected by small-angle scattering, θ_m is the monochromator Bragg angle and k_0 is the nominal wave vector. A certain small fraction r_0 of the incident beam will be small-angle scattered by the cryostat vacuum container and heat shield before reaching the sample. For our purposes, we suppose that we can model the probability for this to occur by a Gaussian function with an angular width ε such that

$$r(\Delta\mathbf{k}_i\to\Delta\mathbf{k}'_i)=\frac{r_0}{(2\pi)^{1/2}k_0\varepsilon}\exp\left[-\frac{(\Delta k'_{iy'}-\Delta k_{iy'})^2}{2\varepsilon^2k_0^2}\right]\times\delta(\Delta k'_{ix'}-\Delta k_{ix'}). \tag{39}$$

The delta function requires the small-angle scattering to be strictly elastic. Thus, the broadened part of $I_0(\Delta\mathbf{k}_i)$ is

$$I_0^b(\Delta\mathbf{k}'_i)\int I_0(\Delta\mathbf{k}_i)r(\Delta\mathbf{k}_i\to\Delta\mathbf{k}'_i)\,\mathrm{d}(\Delta k_{ix'})\,\mathrm{d}(\Delta k_{iy'})=\frac{I_0r_0}{(1+c'_{in}k_0^2\varepsilon^2)^{1/2}}\exp(\tfrac{1}{2}H_{ib}), \tag{40}$$

where

$$H_{ib}=a'_{ib}\Delta k_{ix'}^2+b'_{ib}\Delta k_{ix'}\Delta k_{iy'}+c'_{ib}\Delta k_{iy'}^2, \tag{41}$$

and

$$a'_{ib}=a'_{in}\left(1-\frac{b'_{in}\varepsilon^2k_0^2}{4a'_{in}(c'_{in}\varepsilon^2k_0^2+1)}\right), \tag{42}$$

$$b'_{ib}=b'_{in}/(c'_{in}\varepsilon^2k_0^2+1), \tag{43}$$

$$c'_{ib}=c'_{in}/(c'_{in}\varepsilon^2k_0^2+1). \tag{44}$$

Thus, as $\varepsilon\to 0$, $H_{ib}\to H_{in}$, an obvious result.

The analyzer/detector acceptance function $D(\Delta\mathbf{k}_f)$ will have a form analogous to $I_0(\Delta\mathbf{k}_i)$. We first describe it in the double-primed coordinate system shown in Fig. 8. For the narrow part of $D(\Delta\mathbf{k}_f)$ we have

$$D^n(\Delta\mathbf{k}_f)=t_0D_0\exp(-\tfrac{1}{2}H_{fn}), \tag{45}$$

where

$$H_{fn}=a''_{fn}\Delta k_{fx''}^2+b''_{fn}\Delta k_{fx''}\Delta k_{fy''}+c''_{fn}\Delta k_{fy''}^2. \tag{46}$$

The coefficients a''_{fn}, b''_{fn}, c''_{fn} are related to the Gaussian parameters α_2, α_3 and η_A describing the sample-to-analyzer and analyzer-to-detector collimations and the analyzer-crystal mosaic spread respectively:

$$a''_{fn}=\frac{\tan^2\theta_A}{k_0^2\eta_A^2}+\frac{\sin^2 2\theta_A}{k_0^2\alpha_3^2}, \tag{47}$$

$$b''_{fn}=-\frac{\sin 4\theta_A}{k_0^2\alpha_3^2}-\frac{2\tan\theta_A}{k_0^2\eta_A^2}, \tag{48}$$

$$c''_{fn}=\frac{\cos^2 2\theta_A}{k_0^2\alpha_3^2}+\frac{1}{k_0^2\alpha_2^2}+\frac{1}{k_0^2\eta_A^2}. \tag{49}$$

The Bragg angle of the analyzer is θ_A.

The broad part of $D(\Delta\mathbf{k}_f)$, due to small-angle scattering effects, is given by

$$D^b(\Delta\mathbf{k}_f)=\frac{D_0r_0}{(1+c''_{fn}k_0^2\varepsilon^2)^{1/2}}\exp(-\tfrac{1}{2}H_{fb}) \tag{50}$$

where

$$H_{fb}=a''_{fb}\Delta k_{fx''}^2+b''_{fb}\Delta k_{fx''}\Delta k_{fy''}+c''_{fb}\Delta k_{fy''}^2. \tag{51}$$

The coefficients a''_{fb}, b''_{fb}, c''_{fb} describing this broad distribution are related to the coefficients describing the narrow distribution (a''_{fn}, b''_{fn}, c''_{fn}) by equations identical to (42), (43) and (44) where the single primes are replaced by double primes, and the subscript i is replaced by f. We have explicitly assumed the conventional 'W' configuration of the spectrometer in writing the coefficients in (47), (48) and (49). If the analyzer/detector system is rotated to the antiparallel side of the diffracted beam, the sign of the coefficient b''_{fn} should be reversed.

We now have the task of carring out the four-dimensional integral given in (29) for the counting rate $I_s(\Delta Q_x, \Delta Q_y)$. The expression (33) for $W(\Delta\mathbf{k}_i\to\Delta\mathbf{k}_f)$ contains two delta functions and therefore reduces the four-dimensional integral in (29) to a two-dimensional integral. In order to carry out this integral explicitly, it is necessary to write H_{in}, H_{ib}, H_{fn}, and H_{fb} in the common x-y coordinate frame of Fig. 8, where $\hat{\mathbf{y}}$ is parallel to $\mathbf{G}$ and $\hat{\mathbf{x}}$ is perpendicular to $\mathbf{G}$. This requires a simple coordinate-frame rotation in writing the components of $\Delta\mathbf{k}_i$ and $\Delta\mathbf{k}_f$. If we define a vector

$$\mathbf{p}_{rq}=(a_{rq}, b_{rq}, c_{rq}) \tag{52}$$

consisting of the parameters in the biquadratic form for each of the H's, and a rotation matrix in terms of the sample Bragg angle θ_s,

$$\mathbf{R}(\theta)=\begin{pmatrix}\cos^2\theta_s & -\frac{1}{2}\sin 2\theta_s & \sin^2\theta_s\\ \sin 2\theta_s & \cos 2\theta_s & -\sin 2\theta_s\\ \sin^2\theta_s & \frac{1}{2}\sin 2\theta_s & \cos^2\theta_s\end{pmatrix}, \tag{53}$$

then the coefficients in the common unprimed x-y coordinate frame (Fig. 8) describing the narrow (n) and broad (b) components of the incident (i) and final (f) analyzed beams are given by

$$\mathbf{P}_{in}=\mathbf{R}(\theta_s)\mathbf{P}'_{in}, \tag{54a}$$

$$\mathbf{P}_{ib}=\mathbf{R}(\theta_s)\mathbf{P}'_{ib}, \tag{54b}$$

$$\mathbf{P}_{fn}=\mathbf{R}(-\theta_s)\mathbf{P}''_{fn}, \tag{54c}$$

and

$$\mathbf{P}_{fb}=\mathbf{R}(-\theta_s)\mathbf{P}''_{fb}. \tag{54d}$$

We now have explicit expressions for the four sets of coefficients (a_{rq}, b_{rq}, c_{rq}) describing the narrow and broad components of the incident and diffracted beams in the common x-y coordinate frame, in terms of the instrument parameters α_0, α_1, α_2, α_3, η_A and η_M, the three Bragg angles θ_M, θ_A and θ_s, and the width ε of the small-angle scattering.

After a considerable amount of algebraic manipulation we again find that the counting rate $I_s(\Delta Q_x, \Delta Q_y)$ can be written as the sum of four terms of the form

$$N_h \exp\left[-\frac{(\Delta Q_x - S_h \Delta Q_y)^2}{2\sigma_h^2} - \frac{(\Delta Q_y)^2}{2\mu_h^2}\right], \quad (55)$$

analogous to (22). The first of these terms ($h=0$) is the main Bragg peak coming from Bragg scattering of neutrons (X-rays) in the narrow part of $I_0(\Delta \mathbf{k}_i)$ into the narrow part of $D(\Delta \mathbf{k}_f)$. The second term ($h=1$), giving rise to streak I, is due to neutrons in the narrow part of $I_0(\Delta \mathbf{k}_i)$ Bragg scattering into the broad part of the acceptance function $D(\Delta \mathbf{k}_f)$. The third term, giving rise to streak II, is due to neutrons in the broad part of $I_0(\Delta \mathbf{k}_i)$ Bragg scattering into the narrow part of the acceptance function $D(\Delta \mathbf{k}_f)$. The fourth term ($h=3$) is due to Bragg scattering from the broad part of the incident beam into the broad part of the acceptance function, and is negligibly small.

The parameters σ_h, μ_h and S_h characterizing each of these four Gaussian ($h=0, 1, 2, 3$) components of $I_s(\Delta Q_x, \Delta Q_y)$ are given by

$$\sigma_h = \left(\frac{4\tan^2\theta_s}{u_h} + G^2\eta_s^2\right)^{1/2}, \quad (56)$$

$$\mu_h = \left(\frac{4u_h}{4u_h w_h - v_h^2}\right)^{1/2}, \quad (57)$$

and

$$S_h = \frac{u_h + v_h}{u_h \cot\theta_s}. \quad (58)$$

Here η_s is the sample mosaic spread parameter and G is the magnitude of the reciprocal-lattice vector. The parameters u_h, v_h and w_h depend upon the coefficients (a_{rq}, b_{rq}, c_{rq}) in the biquadratic H's, written in the unprimed x-y coordinate frame:

$$u_h = c_{ig} + c_{fg'} - (b_{ig} + b_{fg'})^2/4(a_{ig} + a_{fg'}) + \frac{2\tan\theta_s}{(a_{ig} + a_{fg'})}(a_{ig}b_{fg'} - b_{ig}a_{fg'} + 2a_{ig}a_{fg'}\tan\theta_s), \quad (59)$$

$$v_h = -2c_{fg'} + b_{fg'}(b_{ig} + b_{fg'})/2(a_{ig} + a_{fg'}) + \frac{\tan\theta_s}{(a_{ig} + a_{fg'})}(b_{ig}a_{fg'} - 3a_{ig}b_{fg'} - 4a_{ig}a_{fg'}\tan\theta_s) \quad (60)$$

and

$$w_h = c_{fg'} - b_{fg'}^2/4(a_{ig} + a_{fg'}) + \frac{\tan\theta_s}{(a_{ig} + a_{fg'})}(a_{ig}b_{fg'} + a_{ig}a_{fg'}\tan\theta_s). \quad (61)$$

The first subscript on the coefficients a, b and c denotes the incident (i) or final (f) diffracted beams. The second subscript, g or g', denotes the narrow (n) or broad (b) components of I_0 and D. The subscripts on u, v and w are ordered such that $h=0$ corresponds to the scattering $I_0^n \to D^n$; similarly $h=1$ corresponds to the scattering process $I_0^n \to D^b$, $h=2$ corresponds to $I_0^b \to D^n$, and finally $h=3$ corresponds to $I_0^b \to D^b$.

Discussion and numerical examples

As anticipated, the results of the calculation in the previous section are algebraically complicated. However, there are a few general conclusions that can easily be made.

(1) Scans transverse to **G** (that is, varying ΔQ_x, at fixed ΔQ_y) will yield three peaks, corresponding to $h=0$ (tail of the main Bragg peak) and $h=1$ and 2 corresponding to streak I and streak II. (The broad $h=3$ peak will, in general, have negligible intensity.) The relative magnitudes of these peaks will depend upon the strength r_0 of the small-angle scattering in the incident and diffracted beams.

(2) The angle $\chi_h/2$ of the streaks is given by

$$\chi_h/2 = \tan^{-1} S_h. \quad (62)$$

If the small-angle scattering in the diffracted beam has a broad distribution (ε large) then the coefficients a_{fb}, b_{fb}, c_{fb} will be small, and v_1 will approach zero. Thus, according to (58), $\chi_1/2$ will approach θ_s. Likewise, if the small-angle scattering in the incident beam has a broad distribution (ε large), then a_{ib}, b_{ib} and c_{ib} are small, and v_2 approaches $-2u_2$, and $\chi_2/2$ approaches $-\theta_s$. Thus, the angle between streak I and streak II asymptotically approaches $2\theta_s$ as ε becomes large.

(3) The sample mosaic spread (η_s) affects only the width (σ_h) of the peaks as observed in transverse scans. It does not affect the orientation (χ_h) of the streaks in reciprocal space, or the rate (μ_h) at which the intensity falls off along the streaks.

The central motivation in carrying out this calculation has been to provide a systematic method for characterizing the weak streaks as a function of the strength r_0 and width ε of the small-angle scattering occurring in the incident and diffracted beams. We show results of selected numerical calculations in Figs. 9 and 10. The angle $\chi/2$ of the streaks in reciprocal space, the transverse width σ of the streaks, and the rate μ at which the scattered intensity drops

off from the Bragg point along the streaks are plotted as a function of the Gaussian width parameter ε characterizing the small-angle scattering. The parameters characterizing the triple-axis spectrometer are given in the figure captions. For Fig. 9, the nominal wavelength is 4·07 Å, and for Fig. 10 the nominal wavelength is 2·35 Å. These wavelengths correspond to conveniently filtered monochromatic neutron beams using Be and pyrolytic graphite, respectively. (A Gaussian width $\varepsilon = 7{\cdot}4$ mrad corresponds to small-angle scattering having a full width at half-maximum FWHM = 17·4 mrad = 1°.) The angle $\chi/2$ saturates at a value equal to the Bragg angle θ_s as ε gets large, as expected. The transverse width σ increases quickly and then levels out at a saturation value, while the parameter μ continues to increase (nearly linearly) with increasing ε, thus showing that the intensity is distributed over a longer segment of the streak as the small-angle scattering broadens. The parameters appropriate to the tail of the main Bragg point correspond to $\varepsilon = 0$ on these plots. In the simple calculation, where we ignored the effects of the angle-wavelength correlations, the predicted ratio of the transverse width of the streaks to the width of the main Bragg peak approaches $2^{1/2}$. Here, this ratio of widths is found to depend on the sample Bragg angle θ_s.

We show in Fig. 11 a series of transverse scans corresponding to the parameters of Fig. 9 (λ = 4·07 Å) for $\theta_s = 35°$ ($G = 1{\cdot}77$ Å^{-1}), and $\varepsilon = 10$ mrad. The monochromator and analyzer are pyrolitic graphite (002), d spacing 3·354 Å, so that $\theta_A = \theta_M$ = 37·35°, and the mosaic spreads $\eta_A = \eta_M = 4{\cdot}94$ mrad (=40′) FWHM. The collimations are 40′-20′-20′-40′ FWHM, and the sample mosaic spread $\eta_s = 0$. We have taken the maximum streak intensity (at $\Delta Q_x = \Delta Q_y = 0$) to be 10^{-4} relative to the central Bragg point. The angle $\chi/2$ of the streaks is 30·4°. It is interesting to note how rapidly these transverse scans evolve from a two-peaked pattern, through a narrow region where three peaks are observed, and into a single rapidly rising central peak (the tail of the main Bragg point).

Fig. 12 shows a map of contours of constant intensity. The parameters used are the same as for Fig. 11. The numbers on the contours are powers of 10. The Bragg point is at $\Delta Q_x = \Delta Q_y = 0$ and is taken to have unit intensity. The units of the axes are Å^{-1}. Since the reciprocal-lattice vector $G = 1{\cdot}77$ Å^{-1} for

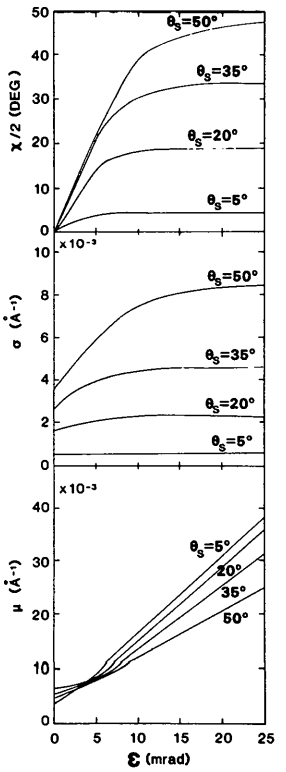

Fig. 9. The three panels show the angle $\chi/2$ of the streaks in reciprocal space, the transverse width σ of the streaks, and the rate μ at which the intensity drops off along the streaks as a function of the Gaussian width ε of the small-angle scattering. θ_s is the sample Bragg angle. The neutron wavelength is 4·07 Å ($k_0 = 1{\cdot}544$ Å^{-1}). The monochromator and analyzer are pyrolytic graphite (002), with mosaic widths of 40′ FWHM. The triple-axis collimations are 40′-20′-20′-40′ FWHM. The sample mosaic spread $\eta_s = 0$.

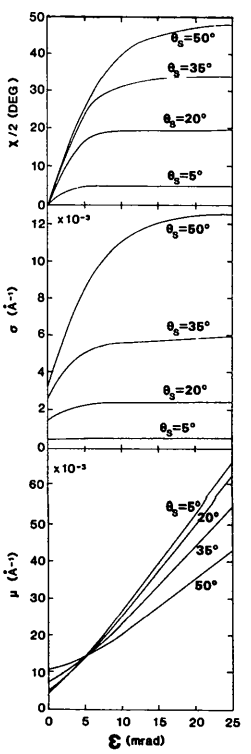

Fig. 10. Numerical results which are analogous to Fig. 9, except here $\lambda = 2{\cdot}35$ Å ($k_0 = 2{\cdot}674$ Å^{-1}), and the collimations are 20′-10′-10′-20′ FWHM.

this example, it is seen that the region of reciprocal space displayed in Fig. 12 is very small.

It has been suggested recently by Pintschovius, Blaschko, Krexner, de Podesta & Currat (1987) that the structure seen by Giebultowicz, Overhauser & Werner (1986) in potassium metal at 4·2 K near the 110 reciprocal-lattice point may be due to this instrumental streaking effect, and not due to charge-density wave (CDW) satellites. This has recently been investigated using an Si crystal by Werner, Giebultowicz & Overhauser (1987) on the same triple-axis spectrometer at the National Bureau of Standards on which the original potassium experiments were done. Structure near the 111 point in Si was observed, but of intensity four times less than in potassium. A final resolution of the correct interpretation of the potassium data will depend upon the outcome of additional future experiments. We hope that the detailed theory of the triple-axis instrumental effects near a Bragg point provided by this paper will be helpful in this task.

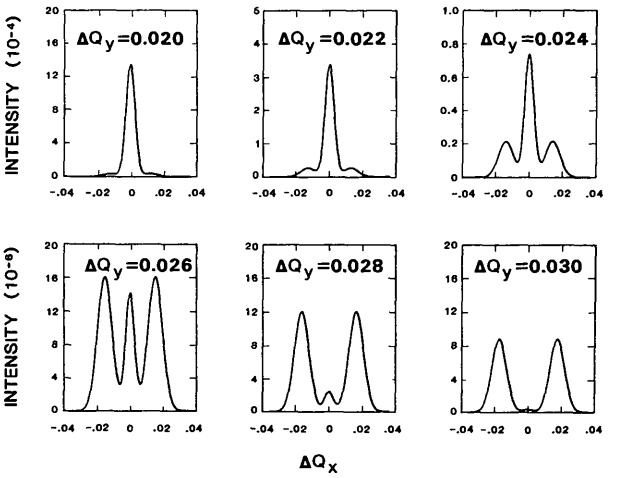

Fig. 11. Transverse scans in the vicinity of a Bragg point. The spectrometer parameters are as given in the caption to Fig. 9. The sample Bragg angle $\theta_s = 35°$, and the Gaussian parameter ε characterizing the small-angle scattering is taken to be 10 mrad. The maximum streak intensity is 10^{-4} of the Bragg-point intensity. For this example, the parameters in expression (55) characterizing the intensity are: $\sigma_0 = 2{\cdot}75 \times 10^{-3}$ Å^{-1}, $\mu_0 = 5{\cdot}5 \times 10^{-3}$ Å^{-1}, $S_0 = 0$; $\sigma_1 = \sigma_2 = 4{\cdot}47 \times 10^{-3}$ Å^{-1}, $\mu_1 = \mu_2 = 13{\cdot}6 \times 10^{-3}$ Å^{-1}, $S_1 = 0{\cdot}586$ and $S_2 = 0{\cdot}586$.

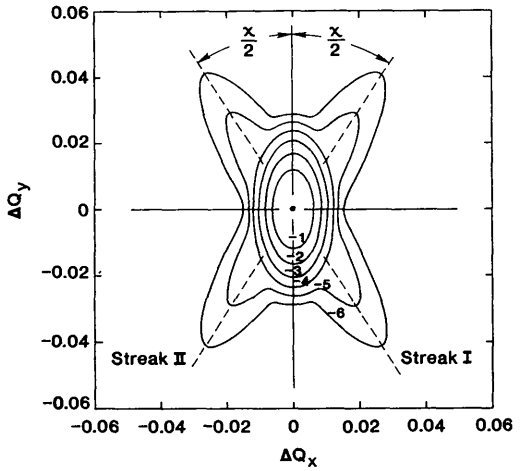

Fig. 12. Contour map of the intensity surrounding the Bragg point. The instrumental parameters used in this calculation correspond to the numbers given in the caption to Fig. 11. The numbers given on the contours are powers of 10. The intensity at the Bragg point ($\Delta Q_x = \Delta Q_y = 0$) is 1·0.

It appears to us that an awareness of the instrumentally generated streaking structure near a Bragg point discussed here may prove to be important in analyzing X-ray experiments designed to observe TDS and Huang scattering.

Finally, we would like to point out that there is another source of instrumentally generated structure near a Bragg point in triple-axis neutron 'inelastic' scans, discussed by Currat & Axe (1978) and by Shirane (1983). Peaks are observed for a triple-axis configuration when two crystals out of the three (monochromator, sample, analyzer) satisfy a Bragg condition for a given neutron energy. For example, there is always a small component of the incident beam which is not exactly of the primary energy E_0, but due to incoherent or inelastic scattering of neutrons of adjacent energies E. At certain (predictable) spectrometer settings, the sample crystal and the analyzer crystal will both be set to Bragg scatter these 'contaminant' neutrons. Processes of this type give rise to a line of singularities (peaks) in $\Delta E - \mathbf{q}$ space, mimicking a phonon dispersion relation terminating at the Bragg point. They can be characterized by the sequence of processes: phonon–Bragg–Bragg. A similar sequence, Bragg–Bragg–phonon, arises from inelastic scattering in the analyzer crystal giving another apparent line of singularities in ΔE–$\mathbf{q}$ space. The sequence Bragg–phonon–Bragg is the 'true' line of singularities due to phonon scattering in the sample. It is important to realize that the physical origin of these spurious 'inelastic' peaks is completely different from the origin of the 'elastic' streaks discussed in this paper.

This work was supported by the National Science Foundation, Physics Division through grant No. NSF-PHY-8410683.

References

COWLEY, R. A. (1987). *Acta Cryst.* A**43**, 824-836.

CURRAT, R. & AXE, J. D. (1978). Research Memo G-106. Brookhaven National Laboratory, Brookhaven, USA.

GIEBULTOWICZ, T. M., OVERHAUSER, A. W. & WERNER, S. A. (1986). *Phys. Rev. Lett.* **56**, 1485-1488.

PINTSCHOVIUS, L., BLASCHKO, O., KREXNER, G., DE PODESTA, M. & CURRAT, R. (1987). *Phys. Rev. B*, **35**, 9330-9332.

SHIRANE, G. (1983). *Physica (Utrecht)*, **120B**, 108-113.

WERNER, S. A., GIEBULTOWICZ, T. M. & OVERHAUSER, A. W. (1987). *Phys. Scr.* T**19**, 266-272.

WERNER, S. A. & PYNN, R. (1971). *J. Appl. Phys.* **42**, 4736-4749.

SHORT COMMUNICATIONS

Contributions intended for publication under this heading should be expressly so marked; they should not exceed about 1000 *words; they should be forwarded in the usual way to the appropriate Co-editor; they will be published as speedily as possible.*

Acta Cryst. (1988). A44, 392-393

Current flow in reflection electron microscopy and RHEED.

By L. D. MARKS and Y. MA, *Materials Research Center, Northwestern University, Evanston, IL* 60208, *USA*

(*Received* 9 *October* 1987, *accepted* 10 *November* 1987)

Abstract

Application of simple Bloch-wave theory to reflection electron microscopy and diffraction leads to inconsistent results - there are not enough boundary conditions to generate a unique solution. To overcome this problem in the past the solution for a thick slab has been used instead of that for a single surface. It is shown that a simpler method valid for a single surface is to insist that only Bloch waves with current flow into or parallel to the crystal surface are allowed. Because of the equations of continuity, this is identical to insisting that only decaying waves are excited in the crystal. An additional feature of this simpler method is that the allowed Bloch waves can be readily represented on a dispersion-surface construction.

In principle the basic analytical solutions for electron diffraction in a material can be directly solved by Bloch-wave methods. Whilst their application to transmission electron microscopy and diffraction is tried and tested, far less has been done to apply them to the important problem of reflection electron microscopy (REM) or reflection high-energy electron diffraction (RHEED). The intention of this note is to point out an important physical point which we have encountered in the process of developing a numerical Bloch-wave program for the reflection case, namely the role of current flow in determining which Bloch waves are excited in the crystal.

The basic theoretical methods for setting up the Bloch-wave solutions can be found in, for instance, the article by Metherell (1975) and will not be repeated here. In a nutshell, the problem reduces to matching from the incident wave vector to the dispersion surface along a line drawn normal to the surface of the crystal, as illustrated in Fig. 1. (We shall not discuss evanescent waves, as they do not play a role in our analysis here, although in reality they must be taken into account in any reasonable model of the diffraction.) If one assumes that the line cuts the dispersion surface, there are *two* possible Bloch waves which can be excited in the crystal for *each* branch of the dispersion surface. Assuming n different branches, we therefore have a maximum of $2n$ different Bloch waves, n different reflected waves and (after matching the wave and its derivative across the crystal surface) a total of $2n$ boundary conditions. As it stands we do not have enough boundary conditions to solve for the Bloch- and diffracted-wave amplitudes.

In the conventional transmission electron diffraction case we solve the analogous problem by insisting that the Bloch-wave vectors must be directed into the crystal. For instance, in the high-energy approximation the wave vectors occur in plus and minus pairs, and we then neglect one of the signs (which depends upon the convention used in defining an incident plane wave). It rapidly became apparent when we tried some numerical tests that this does not work in the reflection electron case. The reason is that the two possible wave vectors for each branch of the dispersion surface need not arise in pairs directed into and out of the crystal, as illustrated in Fig. 1 (see also Table 1). A method proposed by Moon (1972) and by Colella (1972) and Colella & Menadue (1972) is to solve the problem instead for a thick slab with two surfaces rather than just one. Now there are enough boundary conditions, and in the limit of a very thick slab with absorption included only n Bloch waves will be excited within the the crystal.

A simpler method of finding the additional n boundary conditions is to exploit the principle of causality. Physically, the electron beam must travel down the microscope column, reach the crystal surface and then either be reflected or enter the crystal. For any Bloch wave of general form

$$b(\mathbf{r}, \mathbf{k}) = \sum_{g} C_g \exp\left[2\pi i(\mathbf{k}+\mathbf{g}) \cdot \mathbf{r}\right] \qquad (1)$$

the direction of current and energy flow $\mathbf{S}$ (proportional to the expectation value of the Bloch-wave momentum and the group velocity of the Bloch wave and similar to the

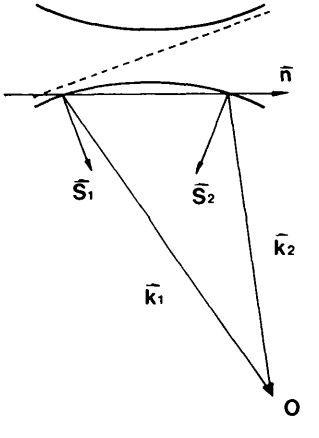

Fig. 1. Illustration of matching from the incoming wave vector to the dispersion surface in the reflection case. For the branch shown, only wave 1 is excited in the crystal, not wave 2, even though the wave vectors for both ($\mathbf{k}_1$ and $\mathbf{k}_2$) are into the crystal, as indicated by the current-flow directions $\mathbf{S}_1$ and $\mathbf{S}_2$.

0108-7673/88/030392-02$03.00